2023-01-1485 Published 15 Jun 2023

Characterization of Atmospheric Icing Conditions during the HALO-(AC)^3 Campaign with the Nevzorov Probe and the Backscatter Cloud Probe with Polarization Detection

Johannes Reinhard Lucke Deutsches Zentrum fur Luft und Raumfahrt

Tina Jurkat German Aerospace Center

Darrel Baumgardner Droplet Measurement Technologies

Frank Kalinka Deutscher Wetterdienst

Manuel Moser, Elena De La Torre Castro, and Christiane Voigt German Aerospace Center

Citation: Lucke, J.R., Jurkat, T., Baumgardner, D., Kalinka, F. et al., "Characterization of Atmospheric Icing Conditions during the HALO-(AC)^3 Campaign with the Nevzorov Probe and the Backscatter Cloud Probe with Polarization Detection," SAE Technical Paper 2023-01-1485, 2023, doi:10.4271/2023-01-1485.

Received: 29 Nov 2022 Revised: 07 Apr 2023 Accepted: 26 Apr 2023

Abstract

The measurement and in-flight characterization of atmospheric icing conditions remains a challenging task. This is due to the large variability of microphysical properties of icing conditions. Icing may occur in pure supercooled liquid clouds of various droplet sizes, it may contain freezing drizzle or freezing rain drops and it also takes place in various types of mixed-phase conditions. A sensor or a combination of sensors to discriminate these icing environments would therefore be beneficial. Especially the phase classification of small cloud particles is still difficult to assess. Within the SENS4ICE project, the German Aerospace Center (DLR) suggests the use of the Nevzorov probe and the Backscatter Cloud Probe with Polarization Detection (BCPD) for the detection and differentiation of icing conditions during research missions that lack standard underwing probes. The first research flights with this instrument combination were conducted in March and April 2022 out of Longyearbyen, Svalbard in the scope of the HALO-(AC)^3 campaign. The Polar 6 aircraft of the Alfred-Wegener-Institut was equipped with the two sensors and other established microphysical cloud probes for validation. Here, we demonstrate our evaluation strategy of the two instruments and show how their data can be used to assess microphysical cloud conditions. We test this evaluation strategy on the basis of one research flight during which a large variety of icing conditions occurred. Furthermore, we also show a comparison of our results to the predictions of the icing warning system ADWICE of the German Weather Service.

Introduction

The accurate and timely assessment of atmospheric icing conditions is essential for the safety of flight for commercial aircraft operation and during research missions. Especially information on the liquid water content (LWC), the particle size distribution (PSD) and the phase of the particles are important [1, 2]. For the detection of atmospheric icing conditions, a variety of sensors can be employed. Hotwire sensors, such as the Nevzorov probe [3, 4, 5] and the WCM-2000 [6] are used for the measurement of LWC and total water content (TWC). For the measurement of the PSD, scattering probes e.g. the Cloud and Aerosol Spectrometer (CAS) [7], the Fast Cloud Droplet Probe (FCDP) [8] and the Cloud Droplet Probe (CDP) [9, 10, 11] are commonly used. If the measurement of particles larger than approximately 50 µm is required, the particle size distribution from the scattering probes is combined with data from optical array probes such as the CIP [7, 12] and the precipitation imaging probe

(PIP) [13]. Typical scattering- and optical array probes are mounted in PMS canisters under the wing or on the fuselage of aircraft and thus cause significant drag. As part of the SENS4ICE (Sensors for Certifiable Hybrid Architectures for Safer Aviation in Icing Environment) project, DLR therefore investigates a combination of the Nevzorov probe and the Backscatter Cloud Probe with Polarization Detection (BCPD) for the detection and differentiation of icing conditions on research aircraft where no underwing cloud probes can be deployed. The BCPD, which is manufactured by Droplet Measurement Technologies (DMT) is advantageous due to its light weight and the fact that it can be integrated into the fuselage imposing no further drag on the aircraft [14]. Furthermore, it features a polarization filter that allows for the differentiation of spherical and aspherical particles. Our version of the Nevzorov probe features an LWC sensor, an 8 mm diameter TWC cone and a 12 mm diameter TWC cone, which is advantageous for the collection of SLD and large ice crystals [5].

During the aircraft field campaign "Arctic Air Mass Transformations during Warm Air Intrusions and Marine Cold Air Outbreaks" (HALO-(AC)³) conducted within the framework of the "Arctic Amplification: Climate Relevant Atmospheric and Surface Processes, and Feedback Mechanisms (AC)³" project [15] a comprehensive in-situ data set of clouds was collected in the vicinity of Svalbard. The collected data set is an ideal test bed for the combination of Nevzorov and BCPD on the Polar 6 aircraft in supercooled droplet and mixed phase conditions in the Arctic, in preparation of the SENS4ICE flight test campaign planned for April 2023.

In this work, we first provide an overview of the instrumentation that is available and then present the data from those instruments obtained during one flight in relevant icing conditions. We assess the performance of the BCPD in detail and discuss corrections that need to be applied to the data. We explain the process of data evaluation from the BCPD and a method to discriminate spherical and aspherical particles. Subsequently we show how we combine the particle number, size and phase information with LWC and TWC measurements from the Nevzorov probe and determine the icing risk. We use data from the established in-situ underwing probes such as the cloud combination probe (CCP) [13] and the PIP for validation and also compare our results to icing predictions of the German Weather Service tool ADWICE [16]. Our sensors and data evaluation procedures provide new strategies for a simplified detection of icing and evaluation of icing forecast tools.

Instrumentation

In this work we use the data of four cloud probes, the BCPD, the Nevzorov probe [3], the CCP and the PIP. The mounting positions of the instruments on the Polar 6 BT-67 aircraft of Alfred-Wegener-Institute can be seen in Figure 1, the setup was very similar to that described in [17, 18]. The CCP, which consists of the Scattering Probe CDP [9, 10, 11] and the Imaging Probe CIP, and the PIP are used to obtain the size

FIGURE 1 Installation locations of the instruments used for this study. The BCPD was located in the fuselage behind a roller-door system that was opened during the flight.

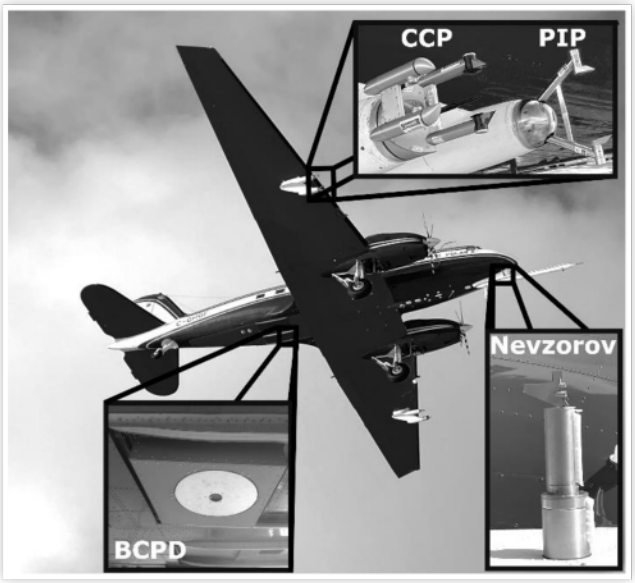

distributions and images that serve as validation to the measurements of the BCPD and as input for collection efficiency corrections for the Nevzorov probe [5]. The Nevzorov probe that was used during this flight campaign was fitted with a sensor head that holds two total water content (TWC) collector cones, one with 8 mm diameter and one with 12 mm diameter. The cone with 12 mm diameter was recently added to the Nevzorov sensor head to provide a larger sample area for the detection of larger ice crystals and SLD, both of which usually occur in low concentrations. The depth of the 12 mm cone was also increased in order to avoid shattering and bouncing effects of large particles [5]. The BCPD is a derivative of the Backscatter Cloud Probe (BCP), which is currently in use on the IAGOS package [19] and has been described in [20]. Compared to the BCP, the BCPD features a polarization filter which allows for the differentiation between spherical and aspherical particles, yet this process is not well described in the literature. The size range of the BCPD extends from 2 to 42 µm. Since the BCPD is a new instrument, we here aim to describe its optical set up and characterize its performance in comparison to established instruments like the CDP and the Nevzorov probe. An overview of all instruments used in this work is given in Table 1.

In almost all works on in-situ cloud measurements, the question arises how measurements should be averaged over time. Too long averaging times tend to blur the observations, while too short averaging times lack statistical significance. We performed experiments where we varied the averaging time for an in-cloud segment and examined the variability of the MVD. We found, that in liquid clouds with a number concentration of approximately 150 cm^{-3} and an MVD of 13 µm an averaging time of five seconds presents the best trade-off between a statistically solid measurement and a high temporal resolution. Details of the investigation are shown in the Appendix. We therefore use a five second average in this

TABLE 1 Microphysics instruments of DLR used during the HALO-(AC)³ campaign aboard the Polar 6 aircraft of Alfred-Wegener Institute.

Instrument	Measured parameter	Range	Reference
Cloud Combination Probe (CCP)	Cloud droplet and ice crystal number, size and shape	2 – 960 µm	[21], [5]
Precipitation Imaging Probe (PIP)	Cloud droplet and ice crystal number, size and shape	100-6400 µm	[22]
Nevzorov Probe	LWC and TWC	0.03 –5 g m^{-3}	[3], [5]
Backscatter Cloud Probe with Polarization Detection	Droplet and ice crystal size and asphericity (phase)	2- 42 µm	

work unless stated otherwise. The five second average is computed with a sliding window, such that averaged data is available for every second.

Overview of the Flight

During a research flight of the Polar 6 aircraft out of Longyearbyen (LYR), Svalbard, that was undertaken on 10 April 2022 as part of the HALO-(AC)³ campaign, multiple occurrences of icing on the aircraft were observed. The weather situation on that day was dominated by a high-pressure system located over the central Arctic and a low-pressure system positioned over Northern Scandinavia. This resulted in winds from east to northeast over the Fram strait. The flight track is shown in Figure 2. The flight is notable because many different cloud types were encountered, with a large variability of cloud water content (CWC) and cloud phase. We therefore find this flight to be ideally suited to assess the sensor's performance in those various conditions. The aircraft first flew west towards Waypoint 1 (WP1), which it reached at 10 UTC. On the track towards WP2 it first encountered very thin clouds and after surpassing WP 6 also thick stratus clouds. During the racetrack pattern between WP 2-5 over the ice, very thin ice clouds were measured. A sawtooth pattern was flown through increasingly thick stratiform mixed-phase clouds between WP5 and WP6. The second racetrack pattern (WP6-9) was parallel to a convergence line. In the north western part of the pattern, stratiform mixed-phase clouds were present, while in the south-eastern part shallow convection was observed by the crew, which resulted in a strong precipitation below the cloud. The racetrack pattern was concluded at approximately 13 UTC and the aircraft headed directly back to LYR from WP9.

A timeline of the microphysical parameters can be seen in Figure 14 in the Appendix. Temperatures varied between -15°C and 0°C. Clouds were generally only encountered below 1000 m altitude. The particle number concentration and the MVD were obtained from a combination of CDP, CIP and PIP measurements. The number concentration attained maximum values of approximately 400 cm^{-3}. The MVD was calculated based on the assumption that all encountered particles were spherical. This assumption does not hold for ice particles, therefore the MVD is not a useful proxy for the predominant particle size. However, in conjunction with the number concentration it is helpful for the interpretation of the data. Segments where the MVD is close to zero but the number concentration is larger than approximately 10 cm^{-3} were dominated by small cloud droplets. On the other hand, if the number concentration is tiny but the MVD is large, thin ice clouds or precipitation were present, as is the case from approximately 10:50 to 11:10. The LWC and TWC were obtained from the Nevzorov probe and collision efficiencies were applied according to the measured droplet size distributions. The procedure of correcting the LWC and TWC measurements of the Nevzorov probe is discussed in detail later in this work. The maximum LWC and TWC that were observed were both approximately 0.7 gm^{-3}.

FIGURE 2 Flight path of the Polar 6 aircraft on 10 April 2022.

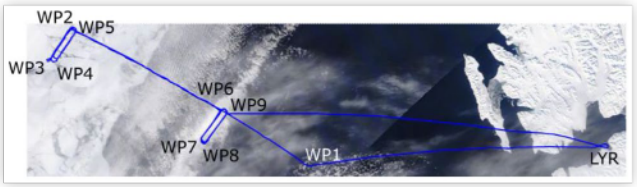

Properties of the BCPD

The BCPD collects light scattered from a solid angle centered around 155° with an apex angle of 18.5°. The incident light is parallel polarized (p-polarized) with respect to the plane spanned by the laser source and the detector (φ = 0, see Figure 3). The width of the beam is approximately 50 µm in x-direction and 250 µm in y-direction. The extent of the sample area in z-direction is approximately 1.1 mm. Scattered light is collected by a lens and then directed on a polarizing beam splitter, which splits it into a p-polarized component

FIGURE 3 Schematic of the BCPD beam geometry.

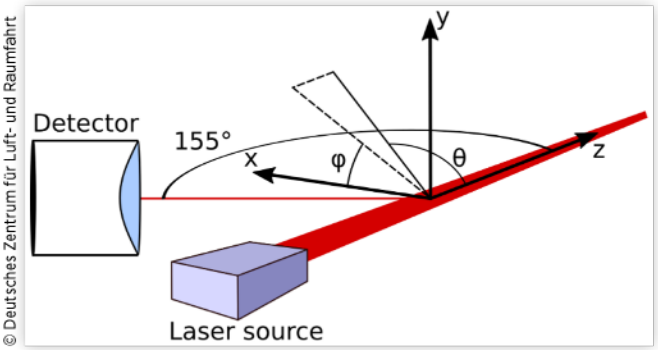

and an s-polarized component (perpendicular to the incident polarization, again, referring to the plane spanned by laser source and detector). The intensity of each of these components is recorded by avalanche photodetectors (one for s-polarized light, one for p-polarized light) as an analog to digital (AD) count. The sum of the two AD counts is used to determine the particle size. We first of all want to show, how the scattering cross section of single particles, which is proportional to the scattered light intensity, behaves for spherical water droplets within the BCPD size range from 2-42 µm diameter.

Mueller calculus [23] is used to obtain the s- and p- polarized components of the scattered light. The calculation is performed with a modified version of the pySCATMECH package [24], which performs the following integration:

$$\mathbf{S_s} = \int_{136.5°}^{173.5°} \int_{-\cos^{-1}\left(\frac{\theta-155°}{18.5°}\right)\frac{18.5°}{\pi}}^{\cos^{-1}\left(\frac{\theta-155°}{18.5°}\right)\frac{18.5°}{\pi}} \mathbf{M}(\theta)\mathbf{R}(\varphi)\mathbf{S_i}\, d\varphi d\theta$$

Here $\mathbf{S_s}$ is the Stokes vector of the scattered light, $\mathbf{S_i}$ is the Stokes vector of the incident light and $\mathbf{M}(\theta)$ is a description of the Mie-scattering behavior for the given droplet size. The rotation matrix $\mathbf{R}(\varphi)$ adjusts the computed Mie scattering response to account for the inclination of the scattering plane with respect to the detector optics for angles of $\varphi \neq 0$. The integration ranges describe the circular area on the scattering sphere from which the BCPD collects the scattered light. The scattering cross sections for p- and s-polarized light are found by multiplying the Stokes vector of the scattered light with Stokes vectors that represent the sensor sensitivities, i.e.:

$$\mathbf{U_\parallel} = \begin{bmatrix} 1 \\ 1 \\ 0 \\ 0 \end{bmatrix}, \mathbf{U_\perp} = \begin{bmatrix} 1 \\ -1 \\ 0 \\ 0 \end{bmatrix}$$

$$\sigma_\parallel = \mathbf{U_\parallel}^T \mathbf{S_s}$$

$$\sigma_\perp = \mathbf{U_\perp}^T \mathbf{S_s}$$

Figure 4 shows the scattering cross sections for s- and p-polarized light for the BCPD. As is to be expected, some depolarization is observed for spherical particles, due to the fact that the BCPD collects light also from solid angles where $\varphi \neq 0$. For these angles the incident light is not purely p-polarized with respect to the scattering plane, hence the overall scattering cross section contains also an s-polarized component. The scattering cross sections (and thus also the backscattered intensity) increase almost monotonously with droplet diameter, but some Mie oscillations [25] are observed at small diameters.

The BCPD does not feature a qualifier, but the slit onto which the scattered light is directed before reaching the polarizing beam splitter selects the most intense portion of the beam. Nonetheless the intensity of the laser beam is not perfectly constant across the sample area of the BCPD.

FIGURE 4 Calculated BCPD scattering cross section for the parallel and perpendicular polarized components of light that is scattered on a spherical water droplet.

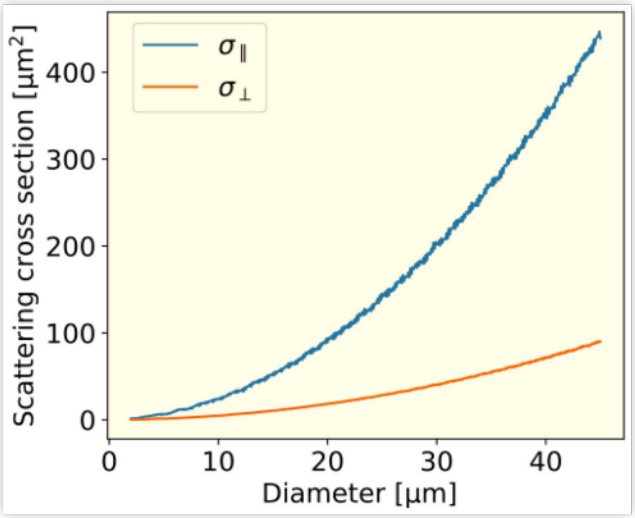

Particles which pass through outer regions of the sample area are therefore undersized. The instrument behavior can be described by the matrix equation $\mathbf{Ax} = \mathbf{y}$ where $\mathbf{y}$ represents the measured size distribution, $\mathbf{x}$ represents the true size distribution which we want to retrieve and $\mathbf{A}$ is a matrix that represents the probability that a particle of size *i* is measured as a particle of size *j* [20]. The sum of a column of $\mathbf{A}$ is therefore less or equal than one. A sum (*S*) smaller than one indicates that (1-*S*)*100 % of particles are undersized so severely that they do not pass the minimum sizing threshold and are thus not recorded at all. The matrix $\mathbf{A}$ therefore automatically accounts for the size dependence of the BCPD sample area. $\mathbf{A}$ is based on a sampling area beam mapping calibration performed at DMT with a droplet generator with 40 µm diameter droplets, similar to the setup described in [9]. The calibration yielded an intensity distribution across the sample area, from which the probabilities of sizing a 40 µm droplet as any different size are computed. The undersizing of droplets with sizes other than 40 µm is computed by simply scaling the intensity distribution observed for 40 µm droplets.

The sample area for 40 µm droplets was measured to be 0.245 mm² (this includes also the fringes where 40 µm droplets are undersized). For 2 µm droplets, the sample area is reduced to less than half of that size, to approximately 0.107 mm². The smaller sample area size for small droplets is not a problem for cloud measurements from a statistical point of view, as small droplets are commonly present in large numbers. In order to obtain realistic size and number concentrations however, a correction for the undersizing behavior of the BCPD is required. The need for such a correction is apparent from Figure 5, which shows that without a correction procedure (gray), the BCPD measures a significantly higher number concentration in the smaller droplet diameter range (<10 µm) than the CDP.

Determining the true size distribution $\mathbf{x}$ is an inverse problem, which is ill-posed [26]. The inverse of matrix $\mathbf{A}$ does not exist and therefore needs to be approximated. Furthermore,

FIGURE 5 Particle size distribution as measured by the CDP and the BCPD. The grey curve represents the BCPD measurement without the inversion applied, while the red curve shows the BCPD measurement after application of the inversion procedure.

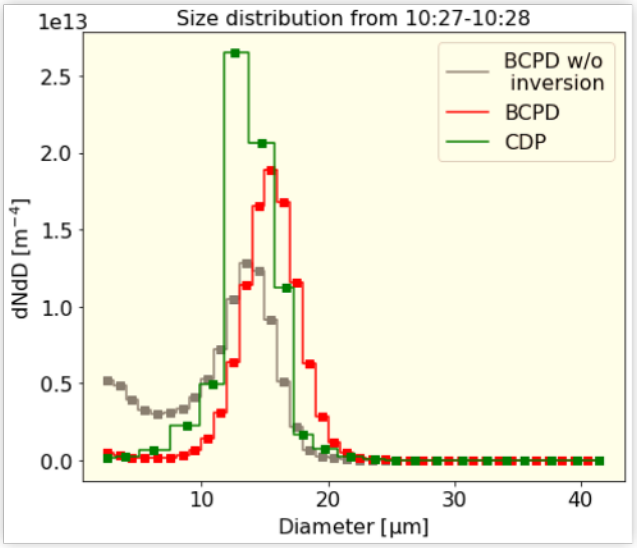

we have a priori knowledge about the solution that needs to be considered; the size distribution must contain only positive values and should be relatively smooth. Such inverse problems have been investigated numerous times, especially in the field of aerosol measurements [27, 28, 29, 30]. For reconstructing size distributions from the BCP, [20] implemented an inversion procedure that was suggested by [31] and improved through the addition of a smoothing step by [32]. The algorithm is often referred to as smooth-Twomey algorithm (STWOM). Here, we also implement STWOM for the correction of the BCPD size distribution and provide details of the procedure and the results in the following.

The BCPD groups particles into 40 size bins, each of which is one µm wide. Hence, the maximum number of measurements m that constitute $\mathbf{y}$ is 40. Atmospheric size distributions may extend over a much wider range, but typical cloud droplet sizes rarely exceed 40 µm. Those that do are usually present in such small numbers that even if they were undersized and recorded by the BCPD, their effect on $\mathbf{y}$ would be minor (although their effect on overall LWC might be significant). Here, we do not aim to reconstruct particle counts of sizes outside the BCPD size range, but limit the extent of $\mathbf{x}$ to the size range of the BCPD from 2-42 µm. The vector $\mathbf{x}$ contains n parameters, which represent the number concentration in 1 µm wide size bins. Hence in our case m=n.

The measured size distributions did not extend across the entire BCPD size range for many segments of the flight that we analyze. Especially the bins corresponding to droplet sizes larger than approximately 30 µm were empty in many instances. This raises the question of how to deal with these bins. It is well possible that particles corresponding to these size bins existed in low numbers, but were undersized by the BCPD and erroneously classified as smaller particles. In principle, an approximation of the number of particles counts in these bins could be obtained from the inversion procedure. However, such an approximation would be somewhat arbitrary, as it is based on no measured counts (i.e., we cannot distinguish if particles of these sizes existed or not). We experimented with such a recovery procedure and found that it produces unrealistically high particle numbers in previously empty bins. We therefore refrain from reconstructing particle counts for all bins with zero counts that lie above the largest size bin with a nonzero count. However, we allow the reconstruction of particle counts in bins with zero counts that are at smaller diameters than the largest size bin with a nonzero count. This reconstruction can be interpreted as smoothing out uncertainties due to the Poissonian variance in the particle counts [33].

The effect of the inversion is demonstrated in Figure 5. The large amount of droplets at sizes smaller than 10 µm is reduced to almost zero and the number concentration in the mode now matches that of the CDP much better. However, the inversion procedure also results in a shift of the mode towards larger diameters, which is not in agreement with the measurement of the CDP. A thorough comparison of BCPD and CDP data follows in the next section.

The quality of the reconstruction can be analyzed by evaluating the residuals $\mathbf{r} = \mathbf{Ax} - \mathbf{y}$. This is shown in Figure 6, where $\mathbf{r}$ is normalized with the reconstructed number of counts to ensure comparability over the BCPD size range. It is apparent, that for diameters up to approximately 25 µm, $\mathbf{y}$ falls within a ±20% interval of the distribution that would be expected when applying matrix $\mathbf{A}$ to the distribution obtained with the inversion procedure. For larger particles the residuals are much greater and for the uppermost size bins exceed -400%, i.e. much more particles are measured than would be expected from the inverted size distribution. However, as mentioned before, the bins where such large errors occurred usually contained only very few particles. Tests of the inversion algorithm on data from wind tunnels, where all size bins contained large numbers of particles show much better agreement for the large size bins. In the next part we show comparisons of the microphysical parameters from the BCPD to those from the CDP and do not observe any effect that could be linked to an underestimation of large particles.

FIGURE 6 Relative residuals remaining in the reconstruction of y from Ax, plotted as an average over all predominantly liquid segments ($\mu_l > 0.8$) of the research flight.

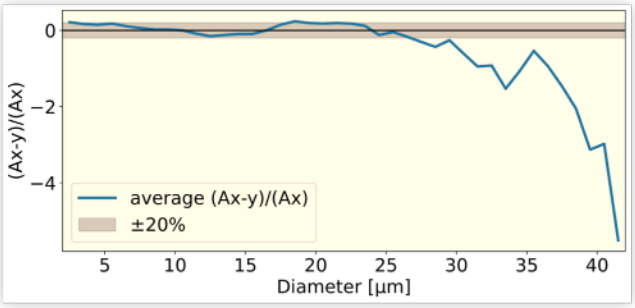

Comparison between BCPD and CDP

The CDP covers a size range similar to that of the BCPD. It is thus an obvious choice to compare its measurement to that of the BCPD. Since the sizing of ice crystals is subject to large uncertainties with both instruments, we limit the comparison to segments where the LWC was at least 80% of the TWC according to the Nevzorov measurements. Furthermore, we only use the overlapping portions of the size distribution of the CDP and the BCPD, i.e. we consider only CDP bins up to 42 µm.

A comparison of the microphysical parameters measured by CDP and BCPD can be seen in Figure 7. It is apparent, that significant discrepancies in number concentration remain between CDP and BCPD despite the correction of undersizing effects of the BCPD. The measured number concentration of the BCPD is most of the time only half of that of the CDP. This phenomenon was observed in all flight campaigns as well as in wind tunnel campaigns. The most likely reason is the measurement position of the BCPD, which is just 2 cm from the aircraft skin, where the airflow is significantly altered and likely slower. The agreement between the MVDs measured by the two instruments is significantly better, and especially in the upper size range falls within the ±20% range. Interestingly, there is almost a 1:1 agreement between the LWCs measured by the two instruments, although with a wide spread. This is likely due to the fact that while the CDP measures significantly more smaller particles than the BCPD, slightly more larger particles which contain a high LWC are detected by the BCPD. These two effects cancel out and lead to matching LWCs between CDP and the BCPD.

FIGURE 7 Comparison of microphysical parameters measured by CDP and BCPD.

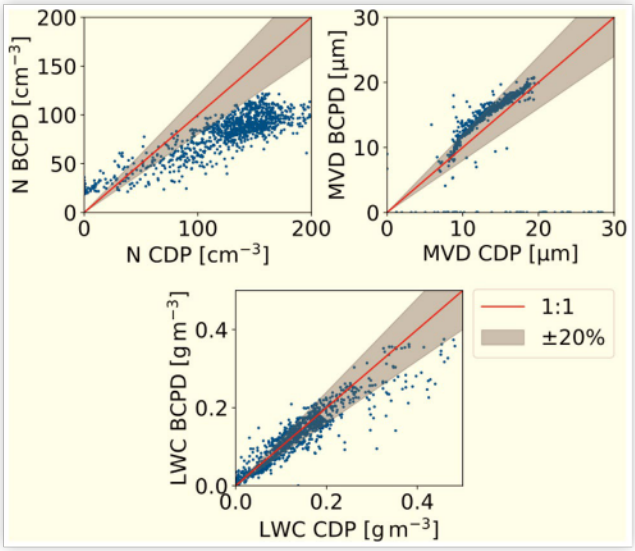

Differentiation of Particle Shape with the BCPD

In most cloud conditions, particle shape is an indication of the phase of the particles, which is a critical parameter e.g. for the identification of icing conditions. Similar as in [34], we define a polarization ratio $\delta = (S-P)/(S+P)$, where S and P are the intensities of the perpendicular and parallel polarized light respectively. It is apparent, that δ can take values between -1 and 1, with -1 indicating 100% p-polarized light and 1 corresponding to 100% s-polarized light. For spherical droplets, δ can be calculated from the respective scattering cross sections, which were computed in the previous section. We observe, that regardless of droplet size, δ has a value of approximately -0.68, with only a small standard deviation of 0.057. In ice clouds, where particles are aspherical, the mean δ is -0.26 but with a very large standard deviation of approximately 0.31 due to the variability of ice particle shape and orientation. The values for water droplets were determined in wind tunnel measurements where the phase of the particles was known, while the values for ice clouds were determined from measurements during the Cirrus-HL campaign [35]. We note that these values are approximations, which underlie small variations depending on the particle size distribution and the type of ice crystals that are present. Furthermore, these ratios only hold for particles with diameters larger than 10 µm. For smaller diameters the small-scale Mie oscillations may lead to δ values anywhere between -1 and 0 for spherical droplets.

Our knowledge on the distribution of the linear polarization parameters allows us to draw conclusions on the asphericity of the particles, from which we deduce the particle phase, i.e. liquid particles are spherical, ice crystals aspherical. We note that some ambiguity exists as we cannot differentiate spherical ice particles from droplets [35].

In order to determine how much ice and how much water is present in a bulk ensemble cloud measurement, we fit the characteristic distributions for ice and water to the overall distribution of δ values (see Figure 8). The areas under the respective curves are then used to estimate the number of spherical and aspherical particles. If the fit parameter for spherical particles is close to zero, this indicates that hardly any liquid phase particles are present, similarly if the fit parameter for aspherical particles is close to zero, the cloud contains hardly any ice.

Shattering of Ice Particles on the Fuselage

The analysis of the particle number concentrations measured by the CDP in the underwing canister as opposed to the measurement of the BCPD at the fuselage brought to light another intriguing effect. While the BCPD usually measured number concentrations lower than the CDP, in conditions with high ice water content the BCPD particle counts significantly exceeded those of the CDP. This is shown in Figure 9. Such conditions were related to the occurrence of a large

FIGURE 8 Distribution of the polarization ratios of all particles measured within a five second interval in a mixed phase cloud (in blue). The peak at -0.68, which corresponds to spherical droplets, is clearly distinguishable. The orange and green lines represent the fit to the degree of linear polarization distribution for spherical and aspherical particles. The areas under the orange and green curves represent the calculated number of particles of water and ice particles, respectively.

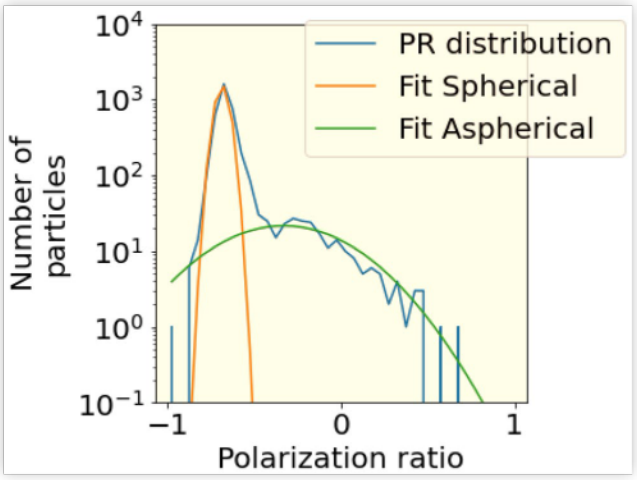

FIGURE 9 Number concentration of the CDP and the BCPD in conditions where the Nevzorov IWC was larger than 90% of the Nevzorov TWC. The right side shows a random sample of particles associated with these conditions.

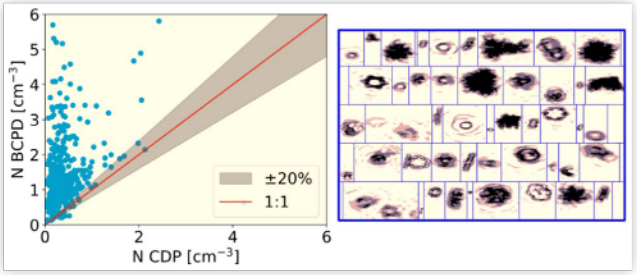

amount of large ice crystals and snowflakes and without small droplets being present. The size of the large ice crystals was outside the measurement range of the BCPD, hence they should not have been detected by the instrument. Therefore, we deduce that the particles measured by the BCPD result from shattering of ice particles on impact with the fuselage. Shattering has been a problem for other cloud instrumentation in the past [36, 37] and has also been mentioned in [20] as a potential cause for abnormally high number concentrations measured by the IAGOS aircraft in cirrus clouds. Usually, shattering events are detected from an analysis of inter-particle times, which are approximately Poisson distributed and related to the particle number concentration [38]. The shattering of a particle causes the almost simultaneous passage of all the splintered fragments and consequently very small inter-particle times. These short inter-particle times manifest themselves as a second mode in the inter-particle time distribution. However, no second mode was detected in the BCPD data, which can be explained by the fact that the particles impact the fuselage significantly ahead and of the BCPD and the fragments then disperse in multiple directions.

The shattering effect makes it impossible to use the BCPD for the detection of ice crystals that actually fall into its size range, since there cannot be certainty, whether an ice particle resulted from a shattering event or not. However, shattering is not necessarily only a disadvantage for the BCPD. In a setup where the BCPD is the only cloud probe on an aircraft, the detection of shattered ice particles at least provides information about the presence of ice crystals, which might otherwise not be detected due to their large size, their low number concentration and the small sample volume of the BCPD.

Correcting LWC and TWC Measurements of the Nevzorov Probe

LWCs and TWCs of the Nevzorov probe need to be corrected for collision efficiency to obtain accurate measurements and information on the cloud phase. Up to now we have used PSDs from the CDP for this correction. Now we want to show, that such a correction can also be accomplished with a satisfactory accuracy with the BCPD data. LWC and TWC from the Nevzorov probe can be computed by solving the system of linear equations given in [39].

$$IWC = \frac{\varepsilon_{l,TWC} W_{LWC} - \varepsilon_{l,LWC} W_{TWC}}{\kappa * \left(\varepsilon_{l,TWC}\beta - \varepsilon_{l,LWC}\varepsilon_{i,TWC}\right)}$$

$$LWC = \frac{\beta W_{TWC} - \varepsilon_{i,TWC} W_{LWC}}{\kappa * \left(\varepsilon_{l,TWC}\beta - \varepsilon_{l,LWC}\varepsilon_{i,TWC}\right)}$$

The equations above contain W_{LWC} and W_{TWC}, the water contents measured by the LWC and TWC sensor respectively. The factor κ is the ratio between the energies needed to heat and evaporate ice and water [3]. The ε_l and ε_i represent the collision efficiencies of the sensors with respect to liquid and ice. The parameter β specifies the residual response to ice of the LWC sensor, which we assume to be 11% regardless of flight condition [40].

The solution of the system of equations is complicated by the fact that the equations contain the sensor collection efficiencies, which depend on the particle size distribution and on the fraction of water and ice that is present in each part of the spectrum. We need information, which part of the particle size spectrum is water and which part is ice. According to [41], in most mixed phase clouds, liquid droplets have diameters between 1 and 50 µm while ice crystal sizes can range from 1 µm to 10^4 µm. Ice crystal number concentrations are usually several orders of magnitude lower than those of liquid droplets. Therefore, as in most studies, we assume that the lower part of the size distribution is entirely liquid, while the upper part is entirely composed of ice particles. This assumption is certainly a simplification, because the possibility exists (and has been observed by e.g [42]), that small ice particles

exist alongside large water drops. However, it is almost certain, that, if present, the liquid particles make up the large majority of the small particles [43]. Nevzorov and BCPD measurements are used to determine this threshold. The liquid fraction of the total water content is easily defined as:

$$\mu_l = 1 - \mu_i = \frac{LWC}{TWC}$$

We implemented an algorithm, which first computes the liquid fraction from the Nevzorov measurements and then computes collision efficiency corrected LWC and TWC values based on that liquid fraction. These two steps are repeated until the changes that occur in LWC and TWC become marginal (see Figure 10). For the LWC sensor the collision efficiency correction suggested for a cylindrical element in [44] is used. The TWC in each step is computed from a combination of the measurement of the 8 mm cone and the 12 mm cone with the collision efficiencies from [45] and [5] respectively applied.

The effect of the collision efficiency correction is visualized in Figure 11. It is apparent, that neglecting sensor collision efficiencies leads to an overestimation of pure supercooled clouds and an underestimate of mixed-phase clouds that contain a small percentage of ice. Both, the collision efficiency derived from the BCPD and that from the CDP can be used to correct this overestimate. The differences in the μ_l values that are computed from the PSDs of the BCPD and of CDP are small; 90% of the time the μ_l values either agreed or fell into the adjacent bin. This demonstrates, that the data from the BCPD is suitable for improving the LWC and TWC measurements of the Nevzorov probe.

FIGURE 10 Flow chart of the collision efficiency correction procedure for the Nevzorov probe measurements. PSDs can from either BCPD or CDP can be used.

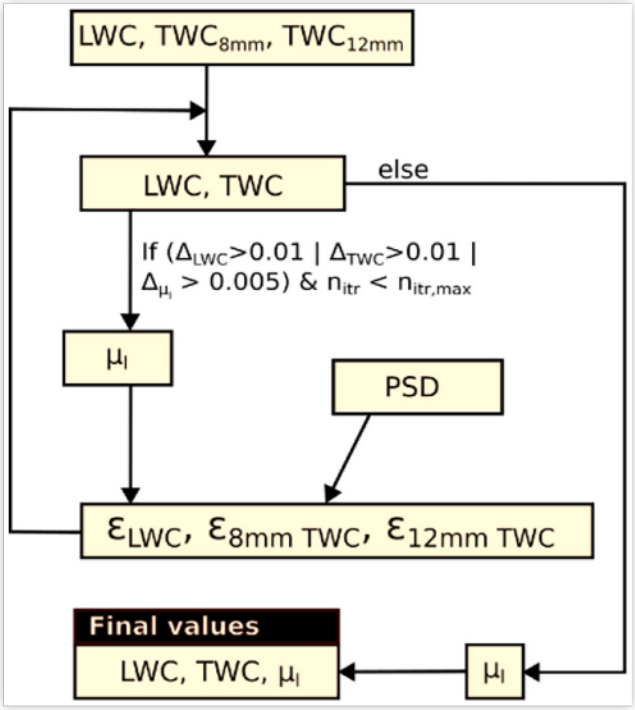

FIGURE 11 Liquid fraction (μ_l) of the TWC from the Nevzorov probe with no collision efficiency applied (left) and collision efficiencies from the BCPD (filled) and from the CDP applied (right).

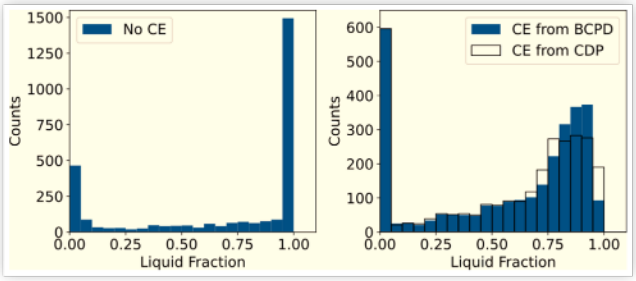

Algorithm for the Assessment of Cloud Phase and Icing Risk

We now present an algorithm that assesses the atmospheric conditions on the basis of measurements of the BCPD and the Nevzorov probe. The algorithm differentiates between five different scenarios:

1. No cloud (NO)
2. Pure ice cloud or solid precipitation (ICE)
3. Convective mixed phase cloud (CMP)
4. Stratiform mixed-phase cloud (SMP)
5. Pure supercooled liquid water cloud (SLC)

We establish the true cloud condition based on measurements from the CDP, CIP and PIP and the Nevzorov. Ice clouds are easily recognized from the ice particles in the images of CIP and PIP and the absence of particles in the CDP. Convective mixed phase conditions contain a large number of ice particles and simultaneously a large number of cloud droplets. We define stratiform mixed-phase clouds as containing only a small number of ice particles but also many cloud droplets. The transition from CMP to SMP is therefore somewhat fluid. Supercooled liquid water clouds are defined as clouds with less than one ice particle per liter, a definition similar to that used in [2] to separate mixed-phase conditions from Appendix O conditions.

The exact parameters used for the distinction can be found in the Appendix. A flow chart of the algorithm is shown in Figure 12. Apart from the cloud phase assessment the algorithm outputs the corrected LWC, TWC and IWC values from the Nevzorov probe, which can be used to assess the risk of icing.

We assessed the performance of the algorithm with a confusion matrix (see Table 2). We investigated 10 instances of each detected condition and compared them to an assessment that we made using the additional information from CDP, CIP and PIP. We find, that out of cloud conditions are always recognized as such. Pure ice conditions were generally also correctly detected, although in a few instances they were

FIGURE 12 Flow chart of the algorithm for the distinction of cloud phase and icing risk.

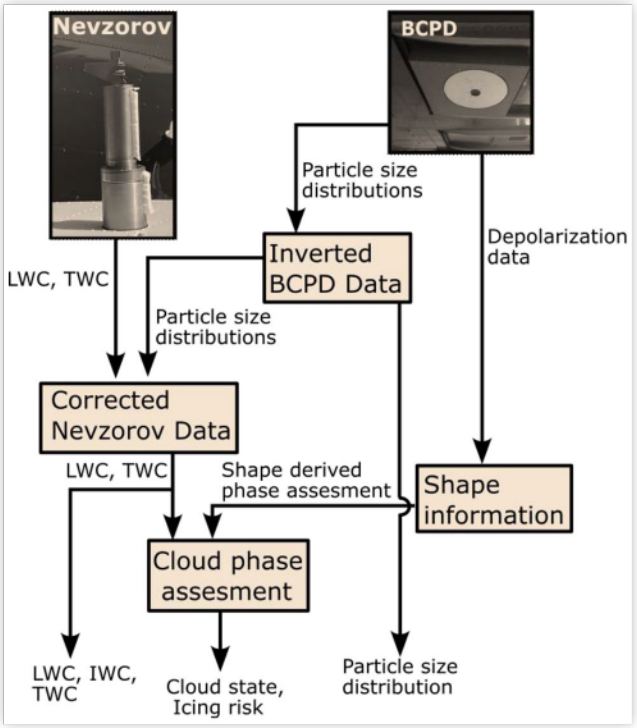

TABLE 2 Confusion matrix for the cloud phase assessment algorithm

True condition \ Detected condition	NO	ICE	CMP	SMP	SLC
NO	9	0	0	0	0
ICE	1	10	1	1	0
CMP	0	0	9	1	0
SMP	0	0	0	6	4
SLC	0	0	0	2	6

confused with either no cloud (when the number concentration was very low), CMP or SMP clouds. The detection of CMP clouds also worked robustly and in just one instance were CMP clouds detected as SMP instead. Significant confusion existed however between SMP clouds and pure liquid water clouds. This can be easily explained by the very small number of ice crystals that are present in SMP conditions. The algorithm we implemented relies on ice particles shattering on the fuselage. If ice particles are so rare that none of the fragments passes the sampling volume, SMP clouds cannot be distinguished from SLC.

Overall, the algorithm can deliver useful information on the cloud phase, which can be used to gain a better statistical understanding of cloud properties. We also find that its results correspond very well with the observations we noted during the flight. We were not able to test the performance of the algorithm for Appendix O conditions, since none were encountered during the HALO-(AC)³ campaign.

Comparison to ADWICE

Our case study provides valuable data for icing occurrence in different cloud situations and can be used for model validation and improvement. For this purpose, we compare our data to the predictions of the in-flight icing warning system (ADWICE) of the German Weather Service (DWD) [16]. We find, that the regions where icing is present (Temperature below 0°C, LWC > 0.01g/m³) are in general well predicted by ADWICE (see Figure 16 in the Appendix). Large scale areas of higher LWC are also correctly forecasted with an increased icing risk. In a few cases however, glaciated clouds are predicted as supercooled liquid clouds. ADWICE is based on threshold values of relative humidity and temperature. As a high relative humidity is a prerequisite also for ice clouds, the differentiation between liquid and ice clouds is challenging for the ADWICE algorithm. Furthermore, ADWICE is a "careful" algorithm, i.e. it favors a false alarm over a missed alarm.

Summary/Conclusions

Our measurements serve as a first test case for airborne deployment of a sensor combination of BCPD and Nevzorov probe that can be used for the assessment of the cloud phase and of the icing risk. The BCPD is a new sensor and this work for the first time establishes procedures for its evaluation. In summary, we can note the following properties of the BCPD:

1. It is lightweight and causes no additional drag to the aircraft
2. Size distributions of the BCPD need to be corrected for undersizing effects. An inversion procedure can be applied to correct this effect, and the procedure yields realistic size distributions. However, because the inversion problem is ill-posed, no perfect reconstruction is possible.
3. There exist large discrepancies between the number concentrations measured by the BCPD and that measured by the CDP, with the BCPD usually measuring a factor two lower concentrations. These discrepancies were observed during all tests that we performed with the BCPD so far, but the reason remains unclear. One possibility, that the location near the fuselage impacts the flow of droplets.
4. The agreement between the measured MVDs of CDP and BCPD on the other hand is within ±20% once MVDs exceed 15 µm. Between 10-15 µm the BCPD measures MVDs which are approximately 20% higher than that of the CDP.
5. The fraction of liquid and ice particles can be determined by fitting two functions two the

distribution of the polarization ratio measured by the BCPD.

6. The BCPD suffers from shattering effects on the fuselage. Caution must therefore be taken when interpreting measurements of the BCPD which show large numbers of small ice particles, as these particles are very likely fragments of larger ice particles. The shattering effect cannot be detected from an inter-particle time analysis.
7. BCPD size distributions can be used to correct the Nevzorov probe for collision efficiency effects. The data from the BCPD produces a similar correction as the CDP data.

Overall, we conclude that while the BCPD certainly has some flaws, which limit its use as a standalone scientific instrument, it can be very helpful in combination with other cloud probes, for example, LWC and TWC measurements of the Nevzorov probe can be significantly improved with the input from the BCPD. This work also demonstrated, that in the given case the icing predictions of ADWICE corresponded well in time and space with the in-situ observations of icing conditions.

References

1. Jeck, R.K., "Icing Design Envelopes (14 CFR Parts 25 and 29, Appendix C) Converted to a Distance-Based Format," 2002.
2. Cober, S.G. and Isaac, G.A., "Characterization of Aircraft Icing Environments with Supercooled Large Drops for Application to Commercial Aircraft Certification," *Journal of Applied Meteorology and Climatology* 51 (2012): 265-284.
3. Korolev, A.V., Strapp, J.W., Isaac, G.A., and Nevzorov, A.N., "The Nevzorov Airborne Hot-Wire LWC–TWC Probe: Principle of Operation and Performance Characteristics," *Journal of Atmospheric and Oceanic Technology* 15 (1998): 1495-1510.
4. Korolev, A., Strapp, J.W., Isaac, G.A., and Emery, E., "Improved Airborne Hot-Wire Measurements of Ice Water Content in Clouds," *Journal of Atmospheric and Oceanic Technology* 30 (2013): 2121-2131.
5. Lucke, J., Jurkat-Witschas, T., Heller, R., Hahn, V. et al., "Icing Wind Tunnel Measurements of Supercooled Large Droplets Using the 12mm Total Water Content Cone of the Nevzorov Probe," *Atmospheric Measurement Techniques* 15 (2022): 7375-7394.
6. Steen, L.-C.E., Ide, R.F., and Zante, J.F.V., "An Assessment of the Icing Blade and the SEA Multi-Element Sensor for Liquid Water Content Calibration of the NASA GRC Icing Research Tunnel," 2016.
7. Baumgardner, D., Jonsson, H., Dawson, W., O'Connor, D. et al., "The Cloud, Aerosol and Precipitation Spectrometer: A New Instrument for Cloud Investigations," *Atmospheric Research* 59-60 (2001): 251-264.
8. Knop, I., Bansmer, S.E., Hahn, V., and Voigt, C., "Comparison of Different Droplet Measurement Techniques in the Braunschweig Icing Wind Tunnel," *Atmospheric Measurement Techniques* 14 (2021): 1761-1781.
9. Lance, S., Brock, C.A., Rogers, D., and Gordon, J.A., "Water Droplet Calibration of the Cloud Droplet Probe (CDP) and In-Flight Performance in Liquid, Ice and Mixed-Phase Clouds during ARCPAC," *Atmospheric Measurement Techniques* 3 (2010): 1683-1706.
10. Lance, S., "Coincidence Errors in a Cloud Droplet Probe (CDP) and a Cloud and Aerosol Spectrometer (CAS), and the Improved Performance of a Modified CDP," *Journal of Atmospheric and Oceanic Technology* 29 (2012): 1532-1541.
11. Faber, S., French, J.R., and Jackson, R., "Laboratory and In-Flight Evaluation of Measurement Uncertainties from a Commercial Cloud Droplet Probe (CDP)," *Atmospheric Measurement Techniques* 11 (2018): 3645-3659.
12. Braga, R.C., Rosenfeld, D., Weigel, R., Jurkat, T. et al., "Comparing Parameterized versus Measured Microphysical Properties of Tropical Convective Cloud Bases during the ACRIDICON–CHUVA Campaign," *Atmospheric Chemistry and Physics* 17 (2017): 7365-7386.
13. Weigel, R., Spichtinger, P., Mahnke, C., Klingebiel, M. et al., "Thermodynamic Correction of Particle Concentrations Measured by Underwing Probes on Fast-Flying Aircraft," *Atmospheric Measurement Techniques* 9 (2016): 5135-5162.
14. Droplet Measurement Technologies, Inc., "Backscatter Cloud Probe with Polarization Detection (BCPD) - Operator Manual," 2020.
15. Wendisch, M., Brückner, M., Crewell, S., Ehrlich, A. et al., "Atmospheric and Surface Processes, and Feedback Mechanisms Determining Arctic Amplification: A Review of First Results and Prospects of the (AC)3 Project," *Bulletin of the American Meteorological Society* 104 (2023): E208-E242.
16. Kalinka, F., Roloff, K., Tendel, J., and Hauf, T., "The In-Flight Icing Warning System ADWICE for European Airspace-Current Structure, Recent Improvements and Verification Results," *Meteorologische Zeitschrift* 26, no. 4 (2017): 441-455.
17. Mech, M., Ehrlich, A., Herber, A., Lüpkes, C. et al., "MOSAiC-ACA and AFLUX - Arctic Airborne Campaigns Characterizing the Exit Area of MOSAiC," *Scientific Data* 9 (2022).
18. Moser M., Voigt C., Jurkat-Witschas T., Hahn V., Mioche G., Jourdan O., Dupuy R., Gourbeyre C., Schwarzenboeck A., Lucke J. und others, "Microphysical and Thermodynamic Phase Analyses of Arctic Low-Level Clouds Measured above the Sea Ice and the Open Ocean in Spring and Summer," *Atmospheric Chemistry and Physics Discussions*, p. 1-27, 2023.
19. Petzold, A., Neis, P., Rütimann, M., Rohs, S. et al., "Ice-Supersaturated Air Masses in the Northern Mid-Latitudes from Regular in situ Observations by Passenger Aircraft: Vertical Distribution, Seasonality and Tropospheric Fingerprint," *Atmospheric Chemistry and Physics* 20 (2020): 8157-8179.
20. Beswick, K., Baumgardner, D., Gallagher, M., Volz-Thomas, A. et al., "The Backscatter Cloud Probe - A Compact Low-Profile Autonomous Optical Spectrometer," *Atmospheric Measurement Techniques* 7 (2014): 1443-1457.
21. Braga, R.C., Rosenfeld, D., Weigel, R., Jurkat, T. et al., "Further Evidence for CCN Aerosol Concentrations Determining the Height of Warm Rain and Ice Initiation in

Convective Clouds over the Amazon Basin," *Atmospheric Chemistry and Physics* 17 (2017): 14433-14456.

22. De La Torre Castro, E., Jurkat-Witschas, T., Afchine, A., Grewe, V. et al., "Differences in Microphysical Properties of Cirrus at High and Mid-Latitudes," *EGUsphere* 2023 (2023): 1-34.
23. Mueller, H., "The Foundation of Optics," *J. Opt. Soc. Am* (1948).
24. National Institute of Standards and Technology, *pySCATMECH,* 2023.
25. Rosenberg, P.D., Dean, A.R., Williams, P.I., Dorsey, J.R. et al., "Particle Sizing Calibration with Refractive Index Correction for Light Scattering Optical Particle Counters and Impacts Upon PCASP and CDP Data Collected during the Fennec Campaign," *Atmospheric Measurement Techniques* 5 (2012): 1147-1163.
26. Tarantola, A., *Inverse Problem Theory and Methods for Model Parameter Estimation* (SIAM, 2005).
27. Kandlikar, M. and Ramachandran, G., "Inverse Methods for Analysing Aerosol Spectrometer Measurements: A Critical Review," *Journal of Aerosol Science* 30 (1999): 413-437.
28. Fiebig, M., Stein, C., Schröder, F., Feldpausch, P. et al., "Inversion of Data Containing Information on the Aerosol Particle Size Distribution Using Multiple Instruments," *Journal of Aerosol Science* 36 (2005): 1353-1372.
29. Sipkens, T.A., Olfert, J.S., and Rogak, S.N., "Inversion Methods to Determine Two-Dimensional Aerosol Mass-Mobility Distributions: A Critical Comparison of Established Methods," *Journal of Aerosol Science* 140 (2020): 105484.
30. Stolzenburg, D., Ozon, M., Kulmala, M., Lehtinen, K.E.J. et al., "Combining Instrument Inversions for Sub-10 nm Aerosol Number Size-Distribution Measurements," *Journal of Aerosol Science* 159 (2022): 105862.
31. Twomey, S., *Introduction to the Mathematics of Inversion in Remote Sensing and Indirect Measurement* (Amsterdam: Elsevier Scientific Publishing Co. (Developments in Geomathematics), 1977), 253.
32. Markowski, G.R., "Improving Twomey's Algorithm for Inversion of Aerosol Measurement Data," *Aerosol Science and Technology* 7 (1987): 127-141.
33. Walser, A., Sauer, D., Spanu, A., Gasteiger, J. et al., "On the Parametrization of Optical Particle Counter Response Including Instrument-Induced Broadening of Size Spectra and a Self-Consistent Evaluation of Calibration Measurements," *Atmospheric Measurement Techniques* 10 (2017): 4341-4361.
34. Baumgardner, D., Newton, R., Krämer, M., Meyer, J. et al., "The Cloud Particle Spectrometer with Polarization Detection (CPSPD): A Next Generation Open-Path Cloud Probe for Distinguishing Liquid Cloud Droplets from Ice Crystals," *Atmospheric Research* 142 (2014): 2-14.
35. Nichman, L., Järvinen, E., Dorsey, J., Connolly, P. et al., "Intercomparison Study and Optical Asphericity Measurements of Small Ice Particles in the CERN CLOUD Experiment," *Atmospheric Measurement Techniques* 10 (2017): 3231-3248.
36. McFarquhar, G.M., Um, J., Freer, M., Baumgardner, D. et al., "Importance of Small Ice Crystals to Cirrus Properties: Observations from the Tropical Warm Pool International Cloud Experiment (TWP-ICE)," *Geophysical Research Letters* 34 (2007).
37. Korolev, A.V., Emery, E.F., Strapp, J.W., Cober, S.G. et al., "Small Ice Particles in Tropospheric Clouds: Fact or Artifact? Airborne Icing Instrumentation Evaluation Experiment," *Bulletin of the American Meteorological Society* 92 (2011): 967-973.
38. Field, P.R., Heymsfield, A.J., and Bansemer, A., "Shattering and Particle Interarrival Times Measured by Optical Array Probes in Ice Clouds," *Journal of Atmospheric and Oceanic Technology* 23 (2006): 1357-1371.
39. Korolev, A. and Strapp, J., "Accuracy of Measurements of Cloud Ice Water Content by the Nevzorov Probe," in *40th AIAA Aerospace Sciences Meeting & Exhibit*, 2002.
40. Korolev A.V., Isaac G.A., Cober S.G., Strapp J.W. and Hallett J., "Microphysical Characterization of Mixed-Phase Clouds," *Quarterly Journal of the Royal Meteorological Society*, vol. 129, p. 39-65, January 2003.
41. Korolev, A., McFarquhar, G., Field, P.R., Franklin, C. et al., "Mixed-Phase Clouds: Progress and Challenges," *Meteorological Monographs* 58 (2017): 5.1-5.50.
42. Lawson, R.P., Woods, S., and Morrison, H., "The Microphysics of Ice and Precipitation Development in Tropical Cumulus Clouds," *Journal of the Atmospheric Sciences* 72 (2015): 2429-2445.
43. Kreidenweis, S.M., Petters, M., and Lohmann, U., "100 Years of Progress in Cloud Physics, Aerosols, and Aerosol Chemistry Research," *Meteorological Monographs* 59 (2019): 11.1-11.72.
44. AC-9C Aircraft Icing Technology Committee, "Calibration and Acceptance of Icing Wind Tunnels (ARP5905)," 2015.
45. Strapp, J.W., Oldenburg, J., Ide, R., Lilie, L. et al., "Wind Tunnel Measurements of the Response of Hot-Wire Liquid Water Content Instruments to Large Droplets," *Journal of Atmospheric and Oceanic Technology* 20 (2003): 791-806.

Contact Information

Johannes.lucke@dlr.de
Phone: +49 (0) 8153283423

Acknowledgments

The SENS4ICE project has received funding from the European Union's Horizon 2020 research and innovation programme under grant agreement number 824253. Furthermore, research performed as part of this worked has received funding from the German Research Foundation (DFG, Deutsche Forschungsgemeinschaft) under the Priority Program SPP PROM Vo1504/5-1. We acknowledge the use of imagery provided by services from NASA's Global Imagery Browse Services (GIBS), part of NASA's Earth Observing System Data and Information System (EOSDIS).

Appendix

Selection of Averaging Time

In order to select an appropriate averaging time, we investigated the effect of the averaging interval on the measured MVD. We examined a cloud segment with a number concentration of approximately 150 cm^{-3} and an MVD of approximately 13 µm (these were typical values during the research flight). We used the observed counts for each size bin as the expectation of a Poisson distribution and drew alternative distributions accordingly. The variation of the MVD for different time intervals can be seen in the Appendix in Figure 13. It is apparent, that sampling for 5 seconds instead of 1 second significantly reduces the variance in the MVD. No large improvement is observed when sampling for an additional 5 seconds. The variance in MVD becomes very small when sampling over 60 seconds, however such a long sampling time does not represent well the MVD measured within the first 10 seconds.

FIGURE 13 MVDs computed from simulated samples over time periods of 1, 5, 10 and 60 seconds. The samples were drawn from a Poisson distribution that used the original number of counts per size bin as the expectation.

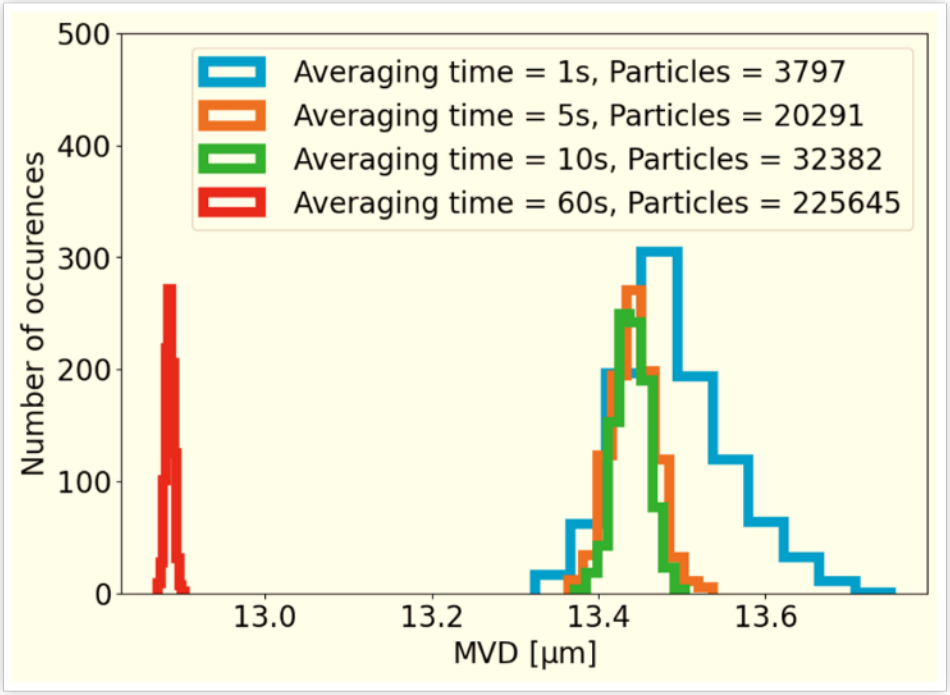

FIGURE 14 Timeline of aircraft and atmospheric parameters. Number concentration and MVD were obtained from a combination of CDP, CIP and PIP, while the LWC and TWC were obtained from the Nevzorov. The beginning and the end of the flight, where no clouds were encountered, were removed from the time series.

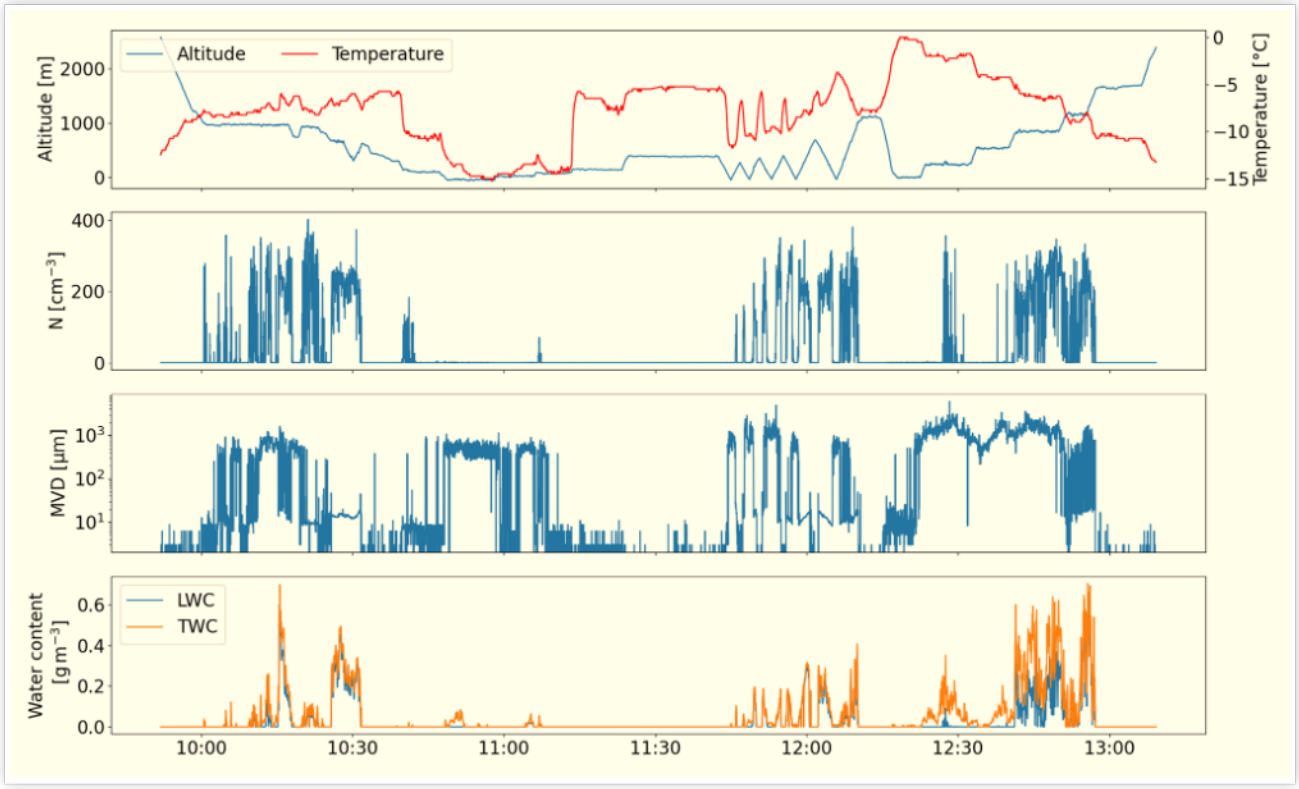

Overview of the Flight

FIGURE 15 Decision tree for the assessment of cloud phase from the BCPD and decision matrix for the overall assessment of cloud phase from BCPD and Nevzorov. Grayed out fields signify that the parameter is not used for the assessment in the given case.

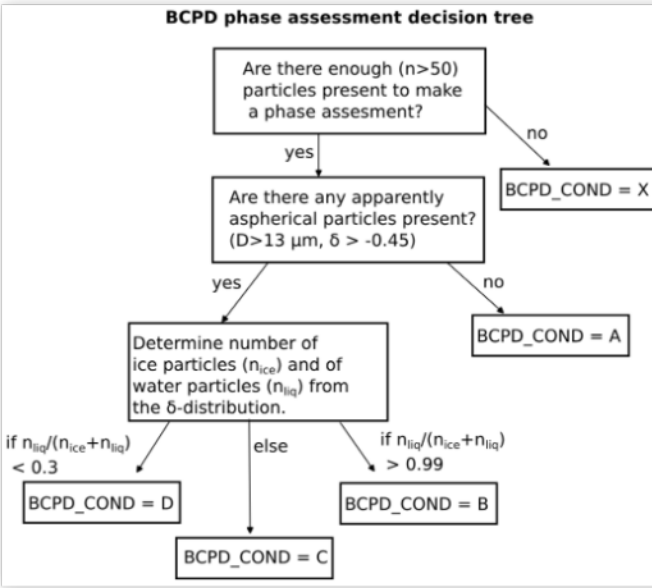

BCPD COND	LWC	TWC	SDR	Cloud condition
X	0	> 0	<=1	ICE
	else			NO
D				ICE
C	0	> 0		ICE
	else			CMP
B	0	> 0		ICE
	else			SMP
A				SLC

Assessment of Cloud Phase

The assessment of cloud phase is performed in two steps (see Figure 15). The first step considers only the BCPD data, while the second step uses the information from the BCPD and the Nevzorov probe. To differentiate between a number of spherical and aspherical particles with the BCPD, we require that the number of particles measured in the five second interval exceeds 50. If this requirement is not fulfilled, the BCPD data is interpreted as being out of cloud (referred to in the decision tree as BCPD_COND X). If there are a sufficient number of particles present, we first analyze if any particle that was detected is clearly aspherical. A particle is clearly aspherical, if its diameter is larger than 13 µm and its polarization ratio is larger than -0.45. For a particle that fulfills these requirements, the possibility of confusion with a spherical particle is minimal. The requirement also means, that we cannot detect the presence and the number of aspherical particles, if there is not a single evidently aspherical particle present.

For the case that no aspherical particles were detected, the BCPD data is interpreted as showing entirely liquid clouds (BCPD_COND A). If aspherical particles are detected, the number fraction of liquid particles is computed and depending on it, a decision between either ice clouds, convective mixed-phase clouds or stratiform mixed-phase clouds is made (BCPD_COND D, C, B respectively).

Afterwards, the data is combined and compared with that of the Nevzorov probe. Cases, where LWC is not detected but TWC is detected by the Nevzorov are generally classified as pure ice clouds / frozen precipitation. Furthermore, the standard deviation ratio (SDR) between the LWC sensor measurement and the 8 mm cone measurement is used to detect thin ice clouds / precipitation with very low number concentrations. Such clouds are difficult to detect simply from the TWC signals, which are very close to zero. From changes in the standard deviation of the 8 mm cone one can detect the impact of single particles. While in clouds with small droplets the standard deviation of the LWC sensor measurement is usually larger than that of the 8 mm cone, in thin ice clouds / precipitation, the standard deviation of the 8 mm cone exceeds that of the LWC sensor.

FIGURE 16 Comparison of LWC and IWC from the Nevzorov probe to the icing severity predicted by ADWICE (LGT = Light, MOD = Moderate, SEV = Severe).

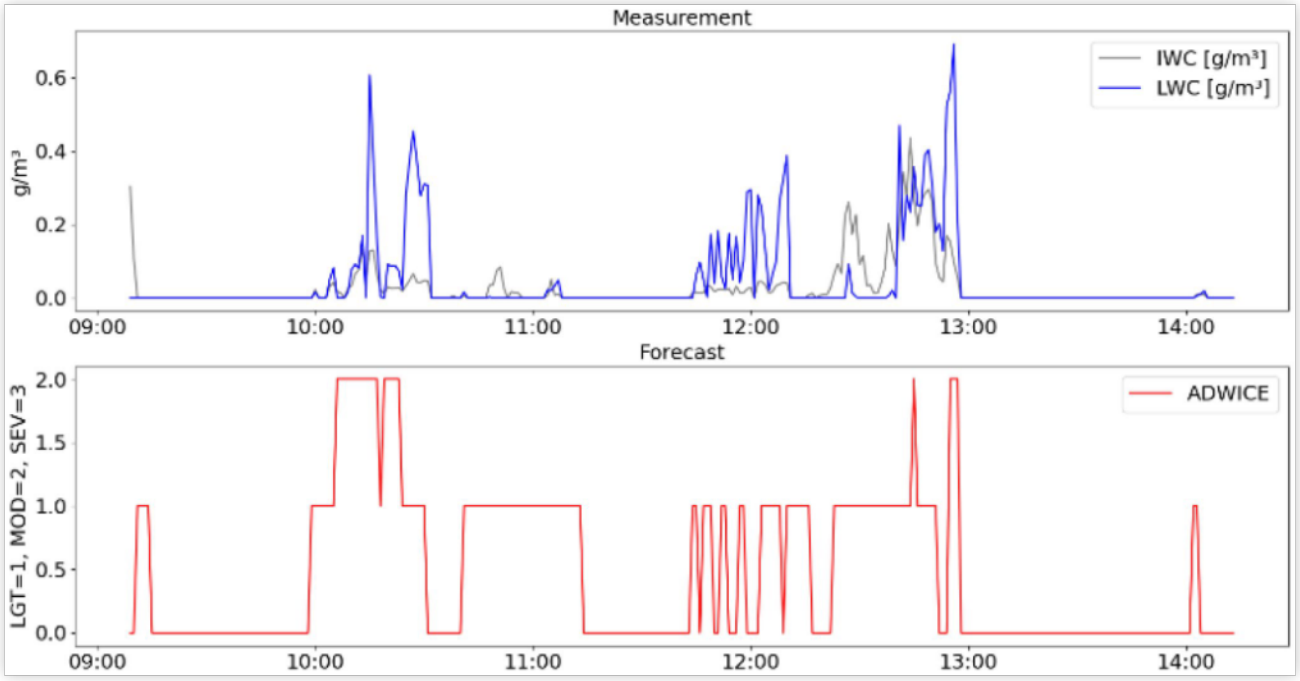

ISSN 0148-7191